Acta Acustica united with Acustica
Vol. 102 (2016) 876 – 892

Scientific Papers
DOI 10.3813/AAA.919002

Time-Domain Simulation of Ultrasound Propagation in a Tissue-Like Medium Based on the Resolution of the Nonlinear Acoustic Constitutive Relations

Noé Jiménez[1)], Francisco Camarena[1)], Javier Redondo[1)], Víctor Sánchez-Morcillo[1)], Yi Hou[2)], Elisa E. Konofagou[2)]

[1)] Instituto de Investigación para la Gestión Integrada de Zonas Costeras, Universitat Politècnica de València, Paranimf 1, 46730 Grao de Gandia, Spain. nojigon@upv.es

[2)] Department of Biomedical Engineering, Columbia University, 351 Engineering Terrace, mail code 8904, 1210 Amsterdam Avenue, New York, NY, USA

Summary

A time-domain numerical code based on the constitutive relations of nonlinear acoustics for simulating ultrasound propagation is presented. To model frequency power law attenuation, such as observed in biological media, multiple relaxation processes are included and relaxation parameters are fitted to both the exact frequency power law attenuation and the empirically measured attenuation of a variety of tissues that does not fit an exact power law. A computational technique based on artificial relaxation is included to correct the non-negligible numerical dispersion of the finite differences method and to improve stability when shock waves are present. The numerical code is especially suitable to study high intensity and focused axisymmetric acoustic beams in tissue-type medium, as it is based on the full constitutive relations that overcomes the limitations of the parabolic approximations, while some specific effects not considered by the Westervelt equation can be also studied. The accuracy of the method is discussed by comparing the proposed simulation solutions to one-dimensional analytical solutions, to k-space numerical solutions, and lastly experimental data from a focused beam propagating in a frequency power law attenuation media.

PACS no. 43.80.Sh, 43.35.Wa, 43.35.Fj

1. Introduction

The significant development of ultrasound technology in the medical field in recent years has led to an increasing demand for realistic simulation tools [1, 2]. Effects like absorption in biological media, nonlinear propagation, heterogeneities, strong focusing, streaming, resonances, multiple scattering or the presence of discontinuities due to tissue layers or rigid boundaries have to be taken into consideration. The most general approach for ultrasound simulation is to directly so the constitutive relations of the nonlinear acoustics. It also allows for the explicit calculation of the particle velocity field, which can be used to compute important quantities such as the vector components of the nonlinear acoustic intensity or the acoustic radiation force [3].

The numerical resolution of the nonlinear constitutive equations in tissue-type medium presents a difficult problem due to the large size of the region of interest in relation to the size of the acoustic wavelength and the complexity of the model. Thus, simplifying assumptions have been needed in the past for modeling beam patterns from ultrasound transducers, as one-way parabolic approximations, most based on the Khokhlov-Zabolotskaya-Kuznetsov (KZK) equation [4, 5, 6, 7, 8, 9, 10, 11]. To overcome the validity limitations of the parabolic approximations, i.e. for large aperture focused sound sources or modeling sound field near the acoustic source, many one-way numerical methods have been proposed, including phenomenological approaches [12, 13] with tissue attenuation [14], or based on the one-way formulation of the Westervelt equation [15, 16].

Tissue inhomogeneity can be modeled in these one-way models [9], like transmission through tissue layers with refraction, but they do not take into account backscattering and multiple reflections. More realistic models, e.g. those accounting for scattering from internal tissue structures, are based on the Westervelt-type full-wave equations [17, 18, 19, 20, 21, 22, 23]. This full-wave equation has been validated for strongly focused sources [24]. However, due to the assumptions underlying the deriva-

Received 28 October 2015,
accepted 6 July 2016.

tion of the Westervelt equation, the accuracy of this model is limited in practical situations as: (*i*) Situations when the particle velocity field becomes rotational. In particular, this case concerns the inclusion of rigid boundaries, where the thermo-viscous boundary layer effects are not-negligible. (*ii*) Situations where the Lagrangian density of acoustical energy do not vanish. The practical situations in which the Lagrangian density is important includes the field near the source or, in general, when plane progressive waves does not exist and the acoustic field becomes complex due to multiple scattering, reverberation or resonances. (*iii*) Practical situations where the period-average particle-velocity is not null, including the self generation of acoustic streaming. See [25] Chap. 3 for a further discussion.

The recent development of computational capacity has enabled consideration of the full constitutive relations (i.e., without the simplifications discussed above). Thus, for small-amplitude acoustic waves, the linearized pressure-velocity formulation of the constitutive relations in inhomogeneous media was solved by means of Finite-Differences in Time-Domain (FDTD) methods with frequency independent losses by Manry *et al.* [26], or using two-step MacCormack finite-differences scheme by Mast et al. [27]. Also, relaxation processes can be included in finite difference methods in an efficient way in order to model tissue attenuation and dispersion [28]. Furthermore, k-space numerical methods have also been applied to solve the linearized first order equations in lossless inhomogeneous media [29]. In order to account for soft tissue losses, the computational solution of the fractional Laplacian by k-space spectral methods have demonstrated to be extremely efficient due to the spatial frequency domain representation of the acoustic field [30].

In the case of nonlinear constitutive-relations models, the evolution of the acoustic magnitudes have been simulated in time-domain by means of finite differences schemes such as Dispersion Relation Preserving method (DRP) in ideal fluids and axisymmetric domains [31, 32]. Thermo-viscous losses in finite-differences methods have been widely used, see Sparrow *et al.* [33]. In order to introduce tissue attenuation in the governing equations, time-dependent fractional derivative can be included by convolutional operators. Thus, in [34] an efficient method has been presented. Although the memory requirements can be strongly reduced compared to direct convolutions, the algorithm still employs up to ten auxiliary fields and a memory buffer of three time steps. Furthermore, despite the possible construction of specific causal memory functions that model soft tissue attenuation and dispersion in Navier-Stokes equations is also possible [35], but certain time history must be stored in memory and in this case the computational domain was limited to one dimensional propagation.

In order to overcome those numerical limitations, recently k-space and pseudo-spectral numerical methods have been applied to constitutive relations in nonlinear regime to solve fractional Laplacian operators efficiently [36]. Furthermore, in the case of domains of hundreds of wavelengths, when the cumulative phase error due to numerical dispersion of standard finite-differences schemes is not negligible, those spectral numerical methods have reported an improvement in accuracy of the numerical solution. These two factors, i.e. the negligible numerical dispersion and the efficient resolution of fractional Laplacian operators, have led the spectral methods, and in particular k-space methods [30, 36], to be widely used in practical applications [1, 2].

However, their main limitation is that the implementation of natural space discontinuities due to tissue layers or rigid boundary conditions leads to errors in the reconstruction of the spectral information due to the poor convergence of Fourier series at jumps: the well-known Gibbs oscillations. This kind of error is typically prevented by implementing spatial spectrum filtering [23], which increases the theoretical minimum sampling points per wavelength. In contrast to locally propagating errors in finite difference methods, these errors propagate globally and affect the accuracy across the domain. On the other hand, taking into account the spatial discontinuity due to symmetry boundary condition, axisymmetric domains becomes difficult to model by standard k-space methods, and full 3D domains must be employed even for axisymmetric configurations. It is worth noting here that, except for some excepcional cases, simulations including realistic inhomogeneous media such as biological tissue are generally 3D. These errors can be prevented by means of the recently developed Fourier Continuation (FC) method [37]. However, the discontinuities formed due to shock propagation are still not solved by FC methods and other additional numerical treatment must be applied to correctly describe shock formation, e.g. intensive computations by high order accurate weighted essentially non-oscillatory schemes (FC/WENO) [38]. Nevertheless, the computational time increases by using these intensive numerical techniques and the multiresolution analysis necessary to detect the discontinuities in the domain.

The aim of the present work is to propose a generalization of the constitutive relations of nonlinear acoustics including multiple relaxation processes in a non-convolutional formulation that allows the time-domain numerical solution using an explicit finite-differences numerical scheme. The frequency power-law attenuation has been included by relaxation processes in the same way as it has been applied to generalized Burgers [6], Khokhlov-Zabolotskaya-Kuznetsov (KZK) [6, 7] and Westervelt equations [19], or in modeling thermo-viscous boundary layer dispersion and attenuation effects in tubes and in arrays of Helmholtz resonators [39], but in the present study we apply the relaxation model directly in the constitutive relations. The relaxation parameters have been fitted to both exact frequency power law attenuation and empirically measured attenuation of a variety of tissues that does not fit an exact power law. Two processes were found sufficient to model tissue attenuation with acceptable accuracy

over a frequency range covering about 4 octaves, as it was demonstrated by Yang *et al.* [7].

The computational technique used is a second-order FDTD method. Using a 2-point numerical stencil, the mayor drawback of the FDTD method is its strong dispersion. The dispersion can be mitigated by using high order schemes [31, 32, 40], but in these methods the number of points for the numerical stencil must be increased and, in general, the number of operations per iteration as well. Moreover, in these high-order scheme an additional treatment of boundaries is needed [32, 40]. In this work we propose a numerical technique based on artificial relaxation to control the non-negligible numerical dispersion of the FDTD method. By implementing this technique, the dispersion is mitigated using a 2-point stencil. In addition this approach improves numerical stability when shock waves are present in the solution. The method includes backscattering and arbitrary propagation direction of finite amplitude beams, and can be specially suitable in axisymmetric configurations where the computational resources for full 3D simulations are prohibitive.

The paper is organized as follows: in Section 2 the model equations that describe the problem are exposed, Section 3 describes the computational method presented in this work and in Section 4 the method is validated comparing the numerical results with analytic solutions for linear, smooth and discontinuous nonlinear waves. In Section 5 solutions for frequency power law media are presented and compared with analytic and numerical solutions obtained by k-space methods as benchmark case. Furthermore, an experimental test was presented where a moderately focused beam propagating in castor oil has been modeled. Finally, a high intensity focused source in the high nonlinear regime focusing through a soft-tissue multilayer media is modeled.

2. Generalized nonlinear acoustics model for multiple relaxation media

2.1. Full-wave modeling

The principles of mass and momentum conservation lead to the main constitutive relations for nonlinear acoustic waves, which for a fluid can be expressed as [41]

$$\frac{\partial \rho}{\partial t} = -\nabla \cdot \left(\rho \mathbf{v}\right) \tag{1}$$

and

$$\rho \left(\frac{\partial \mathbf{v}}{\partial t} + \mathbf{v} \cdot \nabla \mathbf{v} \right) = -\nabla p + \eta \nabla^2 \mathbf{v} + \left(\zeta + \frac{\eta}{3} \right) \nabla \left(\nabla \cdot \mathbf{v} \right), \tag{2}$$

where ρ is the total density field, $\mathbf{v}$ is the particle velocity vector, p is the pressure, and η and ζ are the coefficients of shear and the bulk viscosity respectively. The acoustic waves described by this model exhibit viscous losses with quadratic power law dependence on frequency. In order to include a power law frequency dependence on the attenuation, a multiple relaxation model was added into the time domain equations.

The basic mechanism for energy loss in relaxing media is the appearance of a phase shift between the pressure and density fields. This behavior is modeled here as a time dependent relation at the fluid state equation, that for a fluid retaining the material nonlinear effects up to second order can be expressed as [41, 42]

$$p = c_0^2 \rho' + \frac{c_0^2}{\rho_0} \frac{B}{2A} \rho'^2 + \int_{-\infty}^{t} G(t - t') \frac{\partial \rho'}{\partial t} \, \mathrm{d}t, \tag{3}$$

where $\rho' = \rho - \rho_0$ is the density perturbation over the stationary density ρ_0, B/A is the nonlinear parameter, c_0 is the small amplitude sound speed, and $G(t)$ is the kernel associated with the relaxation mechanism. The first two terms of the right hand side of Equation (3) describe the instantaneous response of the medium, where the convolutional third term accounts for the "memory time" of the relaxing media. Thus, by choosing an adequate time function for the kernel $G(t)$ the model can present an attenuation and dispersion response that fits the experimental data of the heterogeneous media. However, the direct resolution of the constitutive relations Equations (1-3) in this integral form is a complex numerical task due to the convolutional operator. Thus, instead of describe $G(t)$ with a specific time domain waveform, the response of the heterogeneous medium can be alternatively described by a sum of N relaxation processes with exponential time dependence as

$$\int_{-\infty}^{t} G(t - t') \frac{\partial \rho'}{\partial t} \, \mathrm{d}t = \sum_{n=1}^{N} G_n * \frac{\partial \rho}{\partial t}, \tag{4}$$

with the n-th order relaxation kernel expressed as

$$G_n(t) = \eta_n c_0^2 \, \mathrm{e}^{\frac{-t}{\tau_n}} H(t), \tag{5}$$

where $H(t)$ is the Heaviside piecewise function $H(t < 0) = 0$, $H(t > 0) = 1$, τ_n is the characteristic relaxation time and η_n is the relaxation parameter for the n-th order process. This last dimensionless parameter controls the amount of attenuation and dispersion for each process as $\eta_n = (c_n^2 - c_0^2)/c_0^2$, where c_n is the sound speed in the high frequency limit associated to n-th order relaxation process, also known as the speed of sound in the "frozen" state [43]. In order to describe relaxation without the need of including a convolutional operator, we shall define a state variable S_n for each process as

$$S_n = \frac{1}{\tau_n} G_n * \rho'. \tag{6}$$

Thus, using the convolutional property $\partial/\partial t(G(t) * \rho'(t)) = \partial G(t)/\partial t * \rho'(t) = G(t) * \partial \rho'(t)/\partial t$, the time derivative of the relaxation state variable obeys the following relation for the n-th order process:

$$\frac{\partial S_n}{\partial t} = \left(-\frac{1}{\tau_n} \frac{\eta_n c_0^2}{\tau_n} \mathrm{e}^{-\frac{t}{\tau_n}} H(t) + \frac{\eta_n c_0^2}{\tau_n} \mathrm{e}^{-\frac{t}{\tau_n}} \delta(t) \right) * \rho', \tag{7}$$

where $\delta(t)$ is the Dirac delta function. Using Equation (6) this relation becomes a simple ordinary differential equation for each process as

$$\frac{\partial S_n}{\partial t} = -\frac{1}{\tau_n} S_n + \frac{\eta_n c_0^2}{\tau_n} \rho'. \tag{8}$$

Using again convolutional properties, we can substitute Equation (8) into Equation (4), and the relaxing nonlinear state Equation (3) becomes

$$p = c_0^2 \rho' + \frac{c_0^2}{\rho_0} \frac{B}{2A} \rho'^2 - \sum_{n=1}^{N} S_n + \sum_{n=1}^{N} \eta_n c_0^2 \rho'. \tag{9}$$

Moreover, if "frozen" sound speed for N mechanisms is defined as $c_\infty^2 = c_0^2(1 + \sum_{n=1}^{N} \eta_n)$, Equzation (9) leads to

$$p = c_\infty^2 \rho' + \frac{c_0^2}{\rho_0} \frac{B}{2A} \rho'^2 - \sum_{n=1}^{N} S_n. \tag{10}$$

The sound speed in the high frequency limit is reduced to the following due to the small scale of the relaxation parameter [41]

$$c_\infty = c_0 \left(1 + \sum_{n=1}^{N} \frac{\eta_n}{2} \right). \tag{11}$$

Note Equation (10) for a mono-relaxing media is equivalent to what can be found in literature [42],

$$p = c_\infty^2 \rho' + \frac{c_0^2}{\rho_0} \frac{B}{2A} \rho'^2 - \int_{-\infty}^{t} \frac{\eta c_0^2}{\tau} \mathrm{e}^{-\left(\frac{t-t'}{\tau}\right)} \rho'(t') \, \mathrm{d}t. \tag{12}$$

Thus, the constitutive relations to solve by means of the numerical method in the nonlinear regime are the continuity Equation (1), the motion Equation (2) and the second order fluid state relaxing Equation (10), where the state variable S_n obeys the relation Equation (8) for the n-th order relaxation process. Although the aim of this work is to model biological media, the generalized formulation presented here can be used to describe the attenuation and hence the dispersion observed in other relaxing media, such as the relaxation processes of oxygen and nitrogen molecules in air or the relaxation associated with boric acid and magnesium sulfate in seawater [43].

2.2. Small amplitude modeling

If small amplitude perturbations are considered, an equivalent derivation of this model can be expressed for multiple relaxation media [28]. Thus, for an homogeneous inviscid relaxing fluid, the linearized continuity and motion Equations (1)–(2) reduces to

$$\frac{\partial \rho}{\partial t} = -\rho_0 \nabla \cdot \mathbf{v} \tag{13}$$

and

$$\rho_0 \frac{\partial \mathbf{v}}{\partial t} = -\nabla p; \tag{14}$$

and linearizing the fluid state Equation (10) we obtain

$$\rho' = \frac{1}{c_\infty^2} \left(p + \sum_{n=1}^{N} S_n \right). \tag{15}$$

These equations can be solved directly in this form, however, if they are expressed in pressure-velocity formulation the density field is no longer necessary and computational effort can be reduced. Thereby, assuming a linear "instantaneous" bulk modulus $\kappa_\infty = \rho_0 c_\infty^2$, substitution of Equation (15) into Equation (13) yields

$$\frac{\partial p}{\partial t} + \sum_{n=1}^{N} \frac{\partial S_n}{\partial t} = -\kappa_\infty \nabla \cdot \mathbf{v}. \tag{16}$$

Then, taking the time derivative of the state variable Equation (8) we get

$$\frac{\partial p}{\partial t} - \sum_{n=1}^{N} \frac{1}{\tau_n} S_n + \rho' \sum_{n=1}^{N} \frac{\eta_n c_0^2}{\tau_n} = -\kappa_\infty \nabla \cdot \mathbf{v}. \tag{17}$$

Next, substituting again the linearized state Equation (15) and arranging terms the linearized continuity equation leads to

$$\frac{\partial p}{\partial t} + p \sum_{n=1}^{N} \frac{\eta_n c_0^2}{\tau_n c_\infty^2} + \sum_{n=1}^{N} \left(\frac{\eta_n c_0^2}{\tau_n c_\infty^2} - \frac{1}{\tau_n} \right) S_n = -\kappa_\infty \nabla \cdot \mathbf{v}. \tag{18}$$

On the other hand, the state evolution equation can be expressed as a function of the acoustic pressure as

$$\frac{\partial S_n}{\partial t} = -\frac{1}{\tau_n} S_n + \frac{\eta_n c_0^2}{\tau_n c_\infty^2} \left(p - \sum_{n=1}^{N} S_n \right). \tag{19}$$

Thus, the linearized governing Equations (14), (18) for a relaxing media are expressed in a pressure-velocity formulation and can be solved together with the coupled state evolution Equation (19) by means of standard finite differences numerical techniques [28]. In this way, lossless linear acoustics equations can be obtained by setting $\eta_n = 0$ or in the limit when the relaxation times $\tau_n \to \infty$. The relaxation behavior described by this linearized model is achieved too by the formulation described by Yuang *et al.* [28], where the relaxation coefficients η_n and the relaxation variable S_n are defined in a different, but analogous way.

3. Numerical solution by finite-difference time-domain

In this section, the numerical techniques for solving the complete set of equations (continuity Equation (1), momentum Equation (2), state Equation (10) and the relaxation Equation (8)) are presented. The numerical method is based on a second order FDTD scheme where multiple relaxation processes are included in order to: first, model the physical attenuation and dispersion at the frequencies

of interests and, second, correct the numerical dispersion and including artificial attenuation to guarantee convergence in nonlinear regime. Moreover the inclusion of relaxation processes in the presented formulation requires only one extra field per relaxation process and no memory buffer is needed.

3.1. Discretization

Cylindrical axisymmetric $\mathbf{x} = (r, z)$ coordinate system is considered in this work, however, the method can be derived in other coordinate systems. In the standard acoustic FDTD method [44, 45], the particle velocity fields are discretized staggered in time and space respect to the density and pressure fields. As shown in Figure 1, an uniform grid is considered, where $r = i\Delta r$, $z = j\Delta z$, $t = m\Delta t$, with Δr and Δz as the radial and axial spatial steps, and Δt as the temporal step.

Centered finite differences operators are applied over the partial derivatives of the governing equations using a 2-point stencil [44, 45]. Spatial interpolation is needed over the off-center grid variables in order to fulfill the conservation principles over each discrete cell of the domain [46]. The r component of Equation (2) is expressed in cylindrical axisymmetric coordinates as

$$\begin{aligned}\frac{\partial v_r}{\partial t} = &-\frac{1}{\rho}\frac{\partial p}{\partial r} - v_r\frac{\partial v_r}{\partial r} - v_z\frac{\partial v_r}{\partial z} \\ &+ \frac{\eta}{\rho}\left(\frac{\partial^2 v_r}{\partial r^2} + \frac{1}{r}\frac{\partial v_r}{\partial r} + \frac{\partial^2 v_r}{\partial z^2} - \frac{v_r}{r^2}\right) \\ &+ \frac{1}{\rho}\left(\zeta + \frac{1}{3}\eta\right)\left(\frac{\partial^2 v_r}{\partial r^2} + \frac{1}{r}\frac{\partial v_r}{\partial r} + \frac{\partial^2 v_z}{\partial r \partial z} - \frac{v_r}{r^2}\right).\end{aligned} \tag{20}$$

Each term of the above expression is approximated by centered finite differences evaluated at $r = (i + \frac{1}{2}) \cdot \Delta r$, $z = (j + \frac{1}{2}) \cdot \Delta z$, $t = (m + \frac{1}{2}) \cdot \Delta t$. This equation can be solved obtaining an update equation for $v_r|_{i+\frac{1}{2},j}^{m+\frac{1}{2}}$. Similarly, the z component of the motion Equation (2) is expressed as

$$\begin{aligned}\frac{\partial v_z}{\partial t} = &-\frac{1}{\rho}\frac{\partial p}{\partial z} - v_r\frac{\partial v_z}{\partial r} - v_z\frac{\partial v_z}{\partial z} \\ &+ \frac{\eta}{\rho}\left(\frac{\partial^2 v_z}{\partial r^2} + \frac{1}{r}\frac{\partial v_z}{\partial r} + \frac{\partial^2 v_z}{\partial z^2}\right) \\ &+ \frac{1}{\rho}\left(\zeta + \frac{1}{3}\eta\right)\left(\frac{\partial^2 v_r}{\partial z \partial r} + \frac{1}{r}\frac{\partial v_r}{\partial z} + \frac{\partial^2 v_z}{\partial z^2}\right).\end{aligned} \tag{21}$$

This equation is approximated by centered finite differences and evaluated at $r = i \cdot \Delta r$, $z = (j+\frac{1}{2}) \cdot \Delta z$, $t = m \cdot \Delta t$. An update equation is obtained solving this equation for $v_z|_{i,j+\frac{1}{2}}^{m+\frac{1}{2}}$. Equation (1) in cylindrical axisymmetric coordinate system is expressed as

$$\frac{\partial \rho}{\partial t} = -\rho\left(\frac{\partial v_r}{\partial r} + \frac{v_r}{r} + \frac{\partial v_z}{\partial z}\right) - v_r\frac{\partial \rho}{\partial r} - v_z\frac{\partial \rho}{\partial z}. \tag{22}$$

Following the same procedure, each term of the above expression is approximated by centered finite differences and evaluated at $r = i \cdot \Delta r$, $z = j \cdot \Delta z$, $t = (m + \frac{1}{2}) \cdot \Delta t$, and the update equation is obtained solving this expression for $\rho|_{i,j}^{m+1}$. A leap-frog time marching is applied to solve Equations (20-22). Finally, Equation (8) is locally solved for $m+1$ by an explicit fourth-order Runge-Kutta method and then Equation 10) is used to update the pressure field. This process is iteratively repeated for each time step until the desired simulation time is reached.

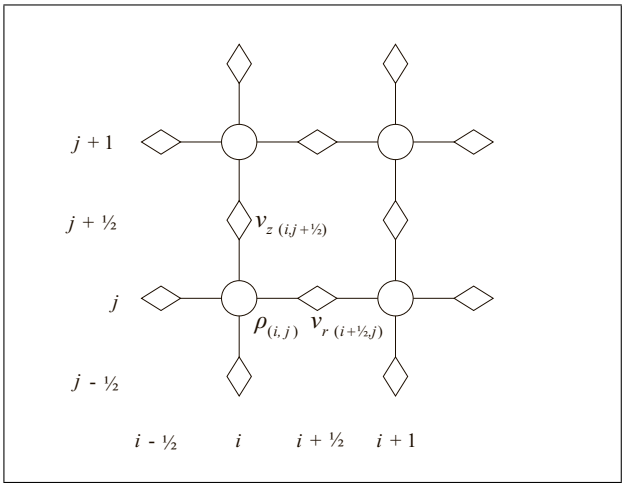

Figure 1. Spatial staggered discretization. The pressure ($p_{i,j}^m$) and the n-th order relaxation process state fields ($S_{n,i,j}^m$) are evaluated at same discrete location as the density ($\rho_{i,j}^m$). Particle velocity fields are discretized staggered in both space and time respect to the density, pressure and the n-th order state fields.

3.2. Boundary conditions

The staggered grid is terminated on velocity nodes, so the boundary conditions are applied on these external nodes, allowing to prevent the singularity of the cylindrical coordinate system: Due to the staggered grid, the only variable discretized at $r = 0$ is v_r, and axisymmetric condition $v_r|_{r=0} = 0$ is applied there. Furthermore, to solve spatial differential operators at boundaries some "ghost" nodes must be created with the conditions: $v_r(-r) = -v_r(r)$, $v_z(-r) = v_z(r)$, $\rho(-\rho(r)$ and $p(-r) = p(r)$.

Perfectly matched layers (PML) [47] were placed in the limits of the domain ($\pm z$ and $+r$) to avoid spurious reflections from the limits of the integration domain. Linearized acoustic equations were solved inside the PML domains using the complex coordinate stretching formulation [48]. For a layer of 30 elements and a broadband incident wave with 1 MHz central frequency and non-normal incidence angle, these absorbing boundary conditions induce here a reflection coefficient of $R = -55.2$ dB. However, the performance of the PML is amplitude dependent as long as the nonlinear terms are uncoupled to the PML domains. The amplitude dependence of the reflection coefficient is shown in Figure 2, where a PML of 25 elements have reported reflection coefficients $R < -50$ dB for waves in linear regime and highly nonlinear waves at normal incidence.

3.3. Minimizing numerical dispersion

The stability for the lossless linear FDTD algorithm follows the Courant-Friedrich-Levy (CFL) condition: for an uniform grid ($\Delta r = \Delta z = \Delta h$) the maximum duration of the time step is limited by $\Delta t \leq \Delta h / c_0 \sqrt{D}$, where D is the dimension number (i.e. $D = 2$ in cylindrical axisymmetric coordinate system). That condition essentially states that for a single time step, information can not propagate in the numerical grid at any distance longer that one cell. However, if relaxation is included numerical instabilities are observed here when $\tau_f / 2\pi < \Delta t$. Due to this empirical relation, the maximum values for relaxation frequencies are also limited by the chosen spatial discretization through the simple relation $f_n < \sqrt{2} N_\lambda f_0$, where $f_n = 2\pi/\tau_n$ is the maximum relaxation frequency for all processes, N_λ is the number of spatial samples per wavelength and f_0 the fundamental frequency.

On the other hand, nonlinear effects induce the progressively growing of harmonics of the fundamental frequency of the initial wave. The diffusive viscous terms in Equation (2) attenuate the small-amplitude high-spatial frequencies, damping the "node to node" numerical oscillations and ensuring numerical stability in weakly nonlinear regime. Thus, for a smooth solution the numerical algorithm shows consistency when $\Delta h \to 0$, so if stability is achieved by the CFL condition, the convergence is guaranteed. However, in strongly nonlinear regime, i.e. when sharp waveforms or even shocks are present in the solution, extra numerical techniques must be employed to guarantee convergence. Artificial viscosity can be added when shock waves are present in the solution. A common implementation follows a fourth order spatial filtering [33, 32]. Thus, the artificial attenuation retrieved by this spatial operator is fourth power of frequency: the low frequency components of the solution remains quasi-undamped, while the higher spatial frequencies are strongly attenuated. In this way, the solution is smoothed and the shock thickness depends on the artificial viscosity coefficient.

However, the main drawback for finite difference methods is numerical dispersion, where the analytic dispersion relation can be expressed in 1D as $\sin^2(k\Delta h/2) = (1/S^2)\sin^2(\omega \Delta t/2)$, with the CFL number $\mathrm{CFL} = c_0 \Delta t / \Delta h$. In this way, numerical dispersion reduces the phase speed of high frequency components, so traveling sharp solutions develop tail oscillations: the low wavenumbers travel fast and leave behind high spatial frequencies. In nonlinear regime, it is well-known that the combined effects of nonlinearity and strong dispersion can lead to rich phenomena, e.g. spatial beatings of the generated harmonics, pulsations on the vertex of a sawtooth wave or soliton formation in strong dispersive media [42]. In this way, the numerical dispersion induced by FDTD methods couple to the physical nonlinearity can lead to a great variety of non-physical or even unstable solutions.

In order to overcome those two limitations, i.e. the generation of harmonics over the discrete limit and the numerical dispersion, we propose the use of artificial relaxation. As shown in Figure 3, physical relaxation introduces *anomalous* dispersion, i.e. the phase speed increases in the high frequency regime, opposite to the numerical (lattice) dispersion of the finite differences scheme. Thus, by introducing a collection of relaxation processes and choosing its adequate relaxation parameters the frequency numerical dispersion can be compensated. As a consequence, introduction of those relaxation processes in the high frequency regime leads to the inevitable inclusion of artificial attenuation. However, this numerical attenuation is then exploited to limit the growing of higher harmonics in a similar way to artificial viscosity [33]. It is worth noting here that using artificial relaxation the frequency dependence of the attenuation is at its maximum a quadratic function of frequency. Therefore, the low frequency range of the solution is also attenuated. Thus, the proposed method is restricted to lossy media.

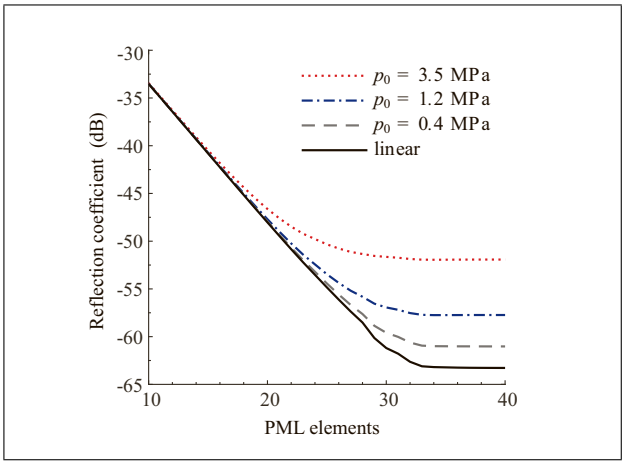

Figure 2. Reflection coefficient of the perfectly matched layer (PML) versus layer thickness for different wave amplitudes. The simulation parameters were $N_\lambda = 25$ points per wavelength, CFL number 0.97, and a sinusoidal excitation with central frequency $f_0 = 1$ MHz in water.

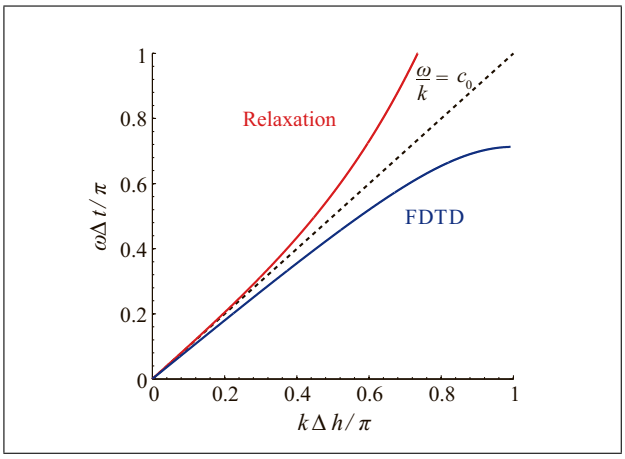

Figure 3. Normalized dispersion relation for of a FDTD lattice of CFL number CFL=0.9 and *anomalous* dispersion relation for a mono relaxing acoustic media. The straight line $c_0 = \omega/k$ represents the reference nondispersive case.

The adequate relaxation parameters that corrects the numerical dispersion have been found by multi-objective optimization techniques, where two cost functions are proposed: one for dispersion and the other one for attenuation. In the first cost function the error between the goal (ideal) dispersion relation and the retrieved numerical dispersion corrected by artificial relaxation is evaluated in the high frequency regime. The second cost function is the error between the desired (ideal) attenuation and the artificial attenuation evaluated in the low frequency regime.

4. Validation

4.1. Single relaxation process

A canonical case of a physical single relaxation process is presented. In order to correct numerical dispersion the parameters of two extra artificial relaxation processes have been found using the multi-objective genetic algorithms provided by the optimization toolbox in MATLAB R2014a v8.03. Linear propagation was considered and simulation parameters were set to typical values for water: $c_0 = 1500$ m/s, $\rho_0 = 1000$ kg/m^3, $B/A = 5$, $\eta = 8.90 \cdot 10^{-4}$ Pa·s. A single physical relaxation process was included, with a characteristic relaxation time of $\tau_1 = 1/2\pi f_0$ and $f_0 = 2$ MHz, and relaxation modulus of $\eta_1 = 0.0678$ that leads to a "frozen" sound speed $c_\infty = 1550$ m/s. In this case, the numerical parameters were set to $\Delta r = \Delta z = 1.87 \cdot 10^{-7}$ m and $\Delta t = 8.65 \cdot 10^{-11}$ s. A plane wave traveling in $+z$ direction was considered.

Thus, the theoretical attenuation for the relaxation processes and including viscosity can be expressed as

$$\alpha(\omega) = \frac{\omega^2}{2\rho_0 c_0^3}\left(\zeta + \frac{4}{3}\eta\right) + \sum_{n=1}^{N} \frac{\eta_n}{2c_0\tau_n}\frac{\omega^2\tau_n^2}{1+\omega^2\tau_n^2}, \quad (23)$$

and the theoretical phase velocity can be predicted as [43]

$$c_p(\omega) = c_0\left(1 + \sum_{n=1}^{N}\frac{\eta_n}{2}\frac{\omega^2\tau_n^2}{1+\omega^2\tau_n^2}\right). \quad (24)$$

In order to compute the attenuation and dispersion of the numerical method, simulated pressure was recorded at two locations z_0 and z_1, and attenuation and phase velocity were estimated from the spectral components over the bandwidth of the input signal. The numerical attenuation was calculated as

$$\alpha(\omega)_{fd} = \frac{\ln\left(|P(\omega, z_1)/P(\omega, z_0)|\right)}{(z_1 - z_0)}, \quad (25)$$

where $P(\omega)$ is the Fourier transform of the measured pressure waveforms at points z_0 and z_1. On the other hand, the phase velocity was computed as

$$c_p(\omega)_{fd} = \frac{\omega \cdot (z_1 - z_0)}{\arg\left(P(\omega, z_1)/P(\omega, z_0)\right)}, \quad (26)$$

where correct phase unwrapping is needed in the arg function.

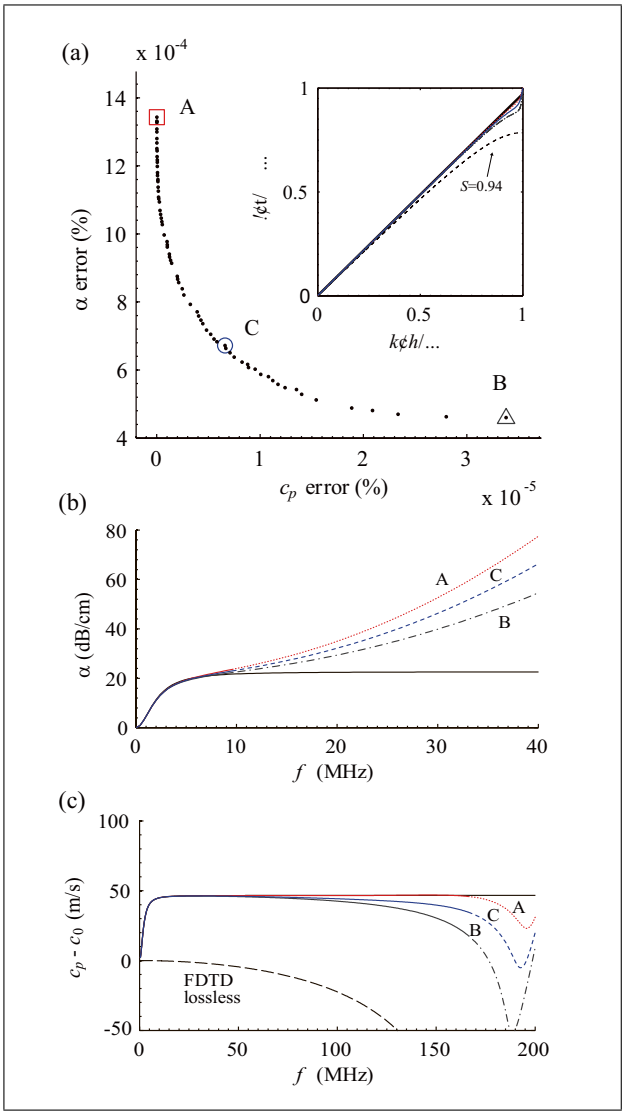

Figure 4. (a) Pareto front retrieved by the multi-objective genetic optimization. Individual (A) is the solution those relaxation parameters minimizes the numerical dispersion. Individual (B) provides the best fit in the attenuation. A compromise between attenuation and dispersion is around the center of the Pareto front (C). Inset in (a) shows the normalized dispersion relation retrieved by the individuals (A) dotted line, (B) dashed-dotted line and (C) continuous line. Dashed black line shows the numerical dispersion relation of the FDTD method without artificial relaxation. The error, i.e. the cost functions, is expressed in percentage. (b) Retrieved attenuation and (c) dispersion by the inclusion of artificial relaxation for the individuals A (dotted), B (dotted-dashed) and C (dashed). Continuous lines represent the frequency range included by the optimization, while dashed lines shows the not optimized frequency range. As a consequence of correcting dispersion, attenuation increases in the high frequency range. This extra attenuation is used as artificial attenuation for numerical-nonlinear stability.

In this way, Figure 4a shows the retrieved Pareto front of the optimization, where 3 different areas can be distinguished. The first area, marked as (A) in Figure 4a, represents individuals whose numerical dispersion is minimal but attenuation is not optimal. On the other hand, the

individuals around area (B) represent a set of relaxation parameters that provides the best agreement between numerical and physical attenuation. A good compromise between both situations can be obtained in the central area of the Pareto front (C), where retrieved attenuation and dispersion in the low frequency band shows good agreement with the physical, and the numerical dispersion has been corrected over a wide frequency range. However, as it can be seen in the inset of Figure 4a, the dispersion relation retrieved by all the cases corrects the FDTD lossless numerical dispersion relation. The phase speed of those three individuals is shown in Figure 4c, where it can be seen that in the frequency range selected for the optimization the numerical phase speed is corrected for all the individuals, where the best fit is obtained for individuals in the Pareto front area A. On the other hand, the inclusion of artificial relaxation leads to an increase of the attenuation in the high frequency range, as is shown in Figure 4a. In this way, as the phase speed error is reduced the effect of artificial attenuation would be increased accordingly. Although this increase can be seen as a non-desired counterpart, the appearance of this extra attenuation is useful in order to control the harmonic growing in nonlinear regime in the same way as artificial viscosity spatial operators [33].

4.2. Nonlinear steady solution for single relaxation process

In order to validate the method in the nonlinear regime a full-wave simulation was developed in a mono-relaxing media using the previously optimized parameters. The lattice parameters were set to $\Delta r = \Delta z = 1.87 \cdot 10^{-7}$ m and $\Delta t = 8.65 \cdot 10^{-11}$ s. The analytical (inverted) solution for the steady solution with $p = -p_0$ for $\tau = -\infty$, $p = p_0$ for $\tau = \infty$ and $p = 0$ for $\tau = 0$, for the retarded time $\tau = t - z/c_0$ reads [49, 25]

$$\tau = \tau_n \ln \frac{\left(1 + p/p_0\right)^{D-1}}{\left(1 - p/p_0\right)^{D+1}} \qquad (27)$$

where $D = \eta_n \rho_0 c_0^2 / 2\beta p_0$ measures the ratio of relaxation effects to nonlinear effects. For $D > 1$, where no shocks are present, the smooth solution retrieved by the FDTD algorithm shows good agreement with the analytical one, and no artificial attenuation is needed. However, for $D < 1$ a discontinuity is present in the solution and convergence is only possible with the inclusion of extra numerical techniques.

Thus, Figure 5a-c shows the analytical and numerical solutions including artificial relaxation and artificial viscosity, where excellent agreement is achieved in all cases. In the case of artificial viscosity (red dotted lines), higher harmonics are strongly attenuated and by reducing grid step convergence can be achieved. As the artificial viscosity operator is essentially a low pass spatial filter, the high wavenumbers of the solution are strongly attenuated and, therefore, a smorthed version of the shock is achieved. However, the phase speed of the higher spatial frequencies

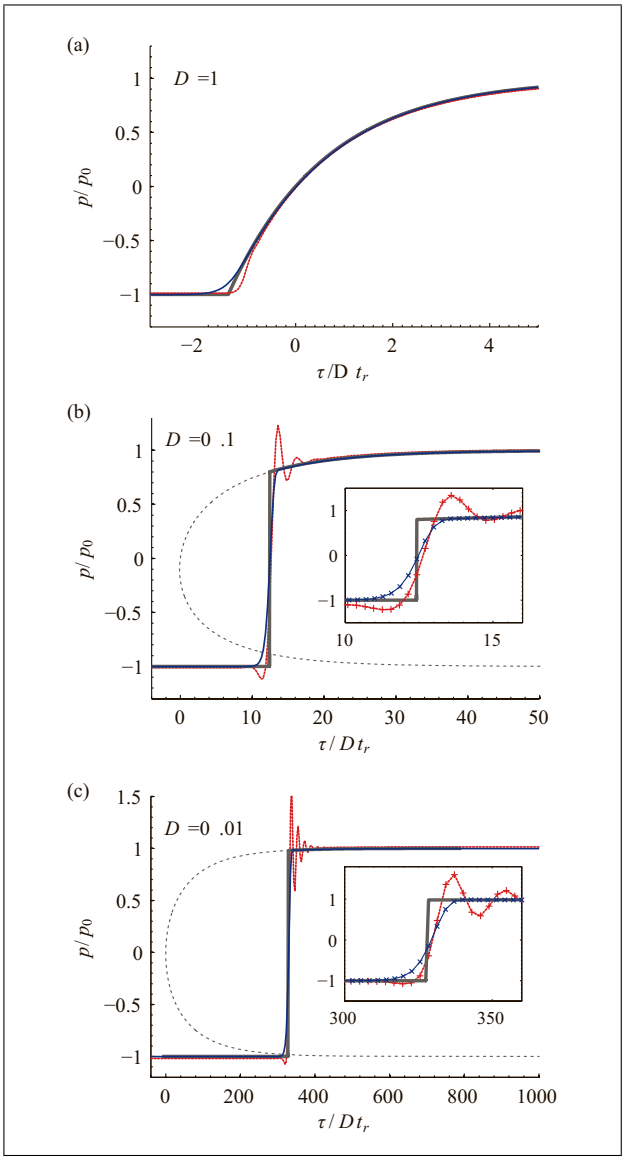

Figure 5. (Colour online) (a) Analytical solution (thick grey line), numerical solution using artificial relaxation with corrected dispersion (continuous line) and using artificial viscosity [33] (dotted line) for the nonlinear steady state solution for $D = 1$. (b) Nonlinear steady state solution for $D = 0.1$. Inset shows detailed shock numerical solution for artificial relaxation (× markers) and artificial viscosity (+ markers). (c) Nonlinear steady state solution for $D = 0.01$.

present in the shock is modified due to the FDTD numerical dispersion. For $D < 1$ (Figure 5b,c) oscillations appear in the tail of the discontinuity, leading to the appearance of a non-physical solution.

On the other hand, the proposed method of artificial attenuation by relaxation also limits the harmonic growing and a smooth version of the shock appears, as shown in blue continuous lines in Figure 5. Moreover, artificial relaxation also corrects phase velocity so all the spatial frequencies travels at same speed and no oscillatory tail appears. The case of $D = 0.01$ is shown in Figure 5c, where nonlinear effects strongly dominate over attenuation. In this case, the oscillations provided by artificial viscosity

increase in amplitude. In contrast, by including artificial relaxation a smoothed version of the shock is captured while accuracy is maintained.

5. Results

5.1. Frequency power law attenuation

Using methodology described above, the optimal relaxation parameters were obtained in order to fit the multiple-relaxation numerical attenuation to frequency power law attenuation in the form

$$\alpha(\omega) = \alpha_0 \omega^{\gamma}, \tag{28}$$

where γ is the power law exponent and α_0 the power law coefficient in Np $(\text{rad/s})^{\gamma}\text{m}^{-1}$. Moreover, the numerical dispersion was corrected by means of artificial relaxation in order to fit the corresponding frequency power law dispersion. Using Kramers–Kronig relations, the analytical form of the power-law dispersion can be expressed as [50]

$$\frac{1}{c_p(\omega)} = \frac{1}{c(\omega_0)} + \alpha_0 \tan\left(\frac{\pi\gamma}{2}\right)\left(|\omega|^{\gamma-1} - |\omega_0|^{\gamma-1}\right). \tag{29}$$

This expression is valid for $0 < \gamma < 3$ with $\gamma \neq 1$, an alternate equation can be found [50] in the limit $\gamma = 1$ as

$$\frac{1}{c_p(\omega)} = \frac{1}{c(\omega_0)} - \frac{2}{\pi}\alpha_0 \ln\left|\frac{\omega}{\omega_0}\right|. \tag{30}$$

The simulation parameters in this case were $c_0 = 1500$ m/s, $\rho_0 = 1000$ kg/m^3, $B/A = 5$, $\eta = 8.90 \cdot 10^{-4}$ Pa·s, $f_0 = 1$ MHz, $\Delta r = \Delta z = 1.3 \cdot 10^{-5}$ m, $\Delta t = 5.4 \cdot 10^{-9}$ s; that leads to 5.7 elements per wavelength at 20 MHz and a CFL number of 0.62. Only two independent relaxation processes were employed in this section to obtain the target frequency power laws.

Following the above procedure, the relaxation times τ_n and relaxation modulus η_n were optimized for different frequency power laws covering the range observed in tissues $\gamma = [1, 1.3, 1.6, 2]$. The attenuation coefficient α_0 was chosen for each power law to present an attenuation $\alpha = 1$ dB/cm/MHz$^{\gamma}$. The fitting was developed over the typical frequency range for medical ultrasound applications, i. e. 1 to 20 MHz for both attenuation and phase speed. The result for the attenuation and phase speed curves are plotted in Figure 6 and Figure 7, where the theoretical and the numerical predictions agree over the frequency range used for the fitting. Note Figure 6 and Figure 7 were generated using the same optimized relaxation parameters and the same numerical parameters.

5.2. Fitting attenuation to tissue experimental data

Although a frequency power law dependence can describe the ultrasound attenuation over a finite frequency range, the attenuation data of some particular tissues shows variation of the exponent over a broad frequency range [51]. Thus, Figure 8 shows experimental attenuation data curves for some tissues where the local slope of the power law

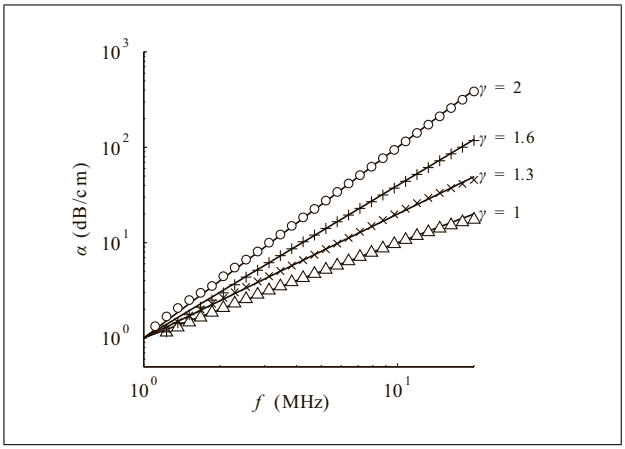

Figure 6. Attenuation retrieved by the numerical algorithm (markers) and target frequency power law attenuation (gray lines). By using the optimization algorithm the relaxation times and modulus were optimized to minimize the relative error between the target power laws of $\gamma = [1, 1.3, 1.6, 2]$ and the attenuation retrieved.

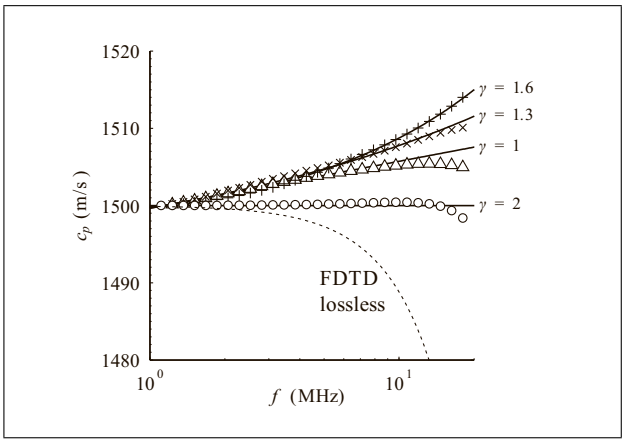

Figure 7. Phase speed retrieved by the numerical algorithm (markers) and target frequency power law attenuation (gray lines) for $\gamma = [1, 1.3, 1.6, 2]$. The optimal relaxation parameters are the same as used in Figure 6.

changes over the measured frequency range. This behavior can be modeled by a sum of relaxation processes by optimizing the relaxation parameter as described above. Thus, the results show that most tissues with locally variable γ can be fitted by only a pair of relaxation processes, in the same way that for constant-slope frequency power law attenuation [6].

Table I shows the error of the numerical attenuation relative to the experimental data. The numerical grid parameters were similar as those presented in previous subsection 5.1. The percent relative error was computed as $\varepsilon = 100/(f_2 - f_1)\int_{f_1}^{f_2}(|\alpha_e(f) - \alpha(f)|)/\alpha_e(f))\text{d}f$, where $\alpha_e(f)$ is the experimental attenuation data, f_1 and f_2 define the frequency range of the measurement. The specific frequency ranges used were ($[f_1, \ f_2]$): [0.3, 3.6] MHz for skull; [1, 5] MHz for tendon; [1, 5] MHz for skin; [1.7, 10] MHz for breast; [1, 9] MHz for liver; [1, 5] MHz

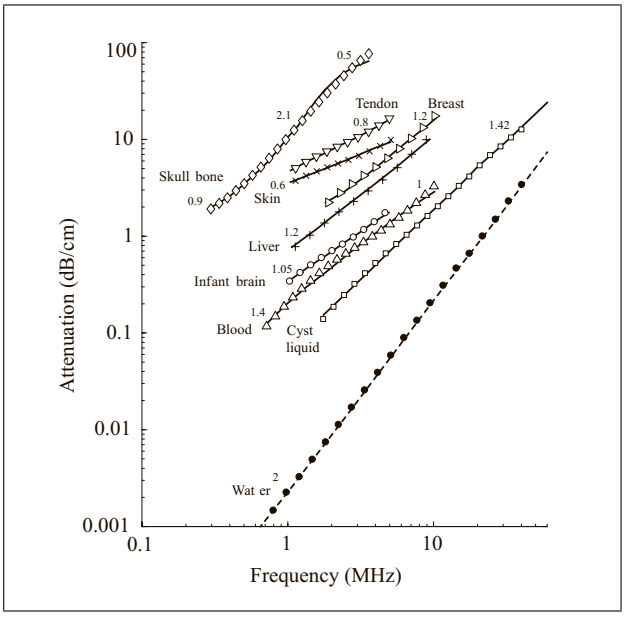

Figure 8. Experimental attenuation data for some tissues adapted from [51] (lines), and obtained by the numerical method (markers) by fitting the parameters of 2 relaxation processes. The numbers above the curves show the exponent of the frequency power law γ for each frequency region (i.e. the slope of the curve).

for brain; [.7, 10] MHz for blood; [1.7, 41] MHz for cyst liquid and [0.5, 40] MHz for water.

As expected, the accuracy of the fit grows as the number of relaxation processes included increases. However, only two processes are enough to obtain relative errors below 1% for tissues with $\gamma < 2$. In the case of tissues where a local value of $\gamma > 2$ has been observed, the fitting procedure fails, like in the skull bone in the 2 MHz range [51]. The maximum slope of the frequency dependent attenuation achieved by single relaxation and thermo-viscous losses is $\gamma = 2$. Therefore, tissues that exhibit a frequency dependent attenuation with a higher slope ($\gamma > 2$) cannot be accurately modeled by a sum of relaxation processes.

From another point of view, Equation (29) states that a frequency power law medium with $2 < \gamma < 3$ presents *standard* dispersion [50], i.e. the phase speed decreases with frequency. On the other hand, *anomalous* dispersion is observed for media falling in the range $0 < \gamma < 2$, i.e. phase speed increases with frequency. Therefore, the dispersion relation of media with $2 < \gamma < 3$ cannot be modeled by a sum of relaxation processes as long as relaxation includes only *anomalous* dispersion. It is worth noting here that no dispersion is observed for the cases $\gamma = 0$ and $\gamma = 2$.

Using the Kramers-Kronig relations [52], the absolute variation of phase speed $\Delta c_p = \left| c_p(f_2) - c_p(f_1) \right|$ can be predicted by the frequency dependent attenuation in a given frequency range. Table II shows the total variation of phase speed observed in the numerical solution and calculated from the Kramers-Kronig relations using the absorption data curves from Figure 8 and using the same frequency ranges listed previously. The magnitude of these

Table I. Error of the optimized attenuation relative to the experimental data for N total relaxation processes.

Tissue	Power law (local slope)	$N = 1$ $\varepsilon(\%)$	$N = 2$ $\varepsilon(\%)$	$N = 3$ $\varepsilon(\%)$	$N = 4$ $\varepsilon(\%)$
Skin	$f^{0.6}$	6.67	0.167	0.136	0.120
Liver	$f^{1.2}$	7.62	0.517	0.404	0.165
Blood	$f^{1.4}$, f^{1}	8.34	0.349	0.330	0.310
Breast	$f^{0.9}$, $f^{1.2}$	5.20	0.216	0.209	0.205
Skull	$f^{0.9}$, $f^{2.1}$, $f^{0.5}$	10.60	10.54	8.628	5.189

Table II. Sound speed variation Δc_p (m/s) for the modeled tissues by means of two relaxation processes and analytical using the Kramers-Kronig relations. Analytical data obtained from [51].

Tissue	Numerical Δc_p	Analytical Δc_p
Skull bone	80.737	70.720
Skin	10.148	10.180
Breast	2.323	3.272
Liver	3.118	2.339
Blood	0.865	0.907

variations are in the order of magnitude of those measured experimentally in this frequency range, and its frequency dependence is roughly linear as observed in real tissues [51].

As expected from the relations between dispersion and absorption [52], for a given power law exponent, the magnitude of the variation in sound speed increases as the total variation of the absorption increases for a given frequency range. In addition, different power-law exponents of the leads to different dispersion curves according to Equations (29)–(30). Moreover, in some real tissues the frequency dependent attenuation do not fit an unique value of the power-law exponent e.g. blood, breast and skull tissues shown in Table II. Therefore, in reality the situation is more complex and not only the magnitude of the attenuation but also the exponent of the power law and its dependence in frequency must be taken into account. We refer to [53] Chapter 8 for a further discussion on the interplay between dispersion, attenuation and nonlinearity in frequency power-law media.

5.3. Nonlinear one-dimensional propagation in tissue-like media

5.3.1. Non-dispersive media

In order to study the convergence of the numerical calculations to an analytical solution of the model in the nonlinear regime, a medium with frequency squared dependence attenuation is implemented using the adequate relaxation times and relaxation modulus as explained above. The numerical solution is compared with the analytical solution for a plane wave traveling through a thermo-viscous fluid proposed by Mendousse [43]. Here, we shall define the Gol'dberg number as $\Gamma = x_a/x_s$, with absorption length $x_a = 1/\alpha_0\omega^\gamma$, shock formation distance $x_s = 1/\beta\varepsilon k$ and

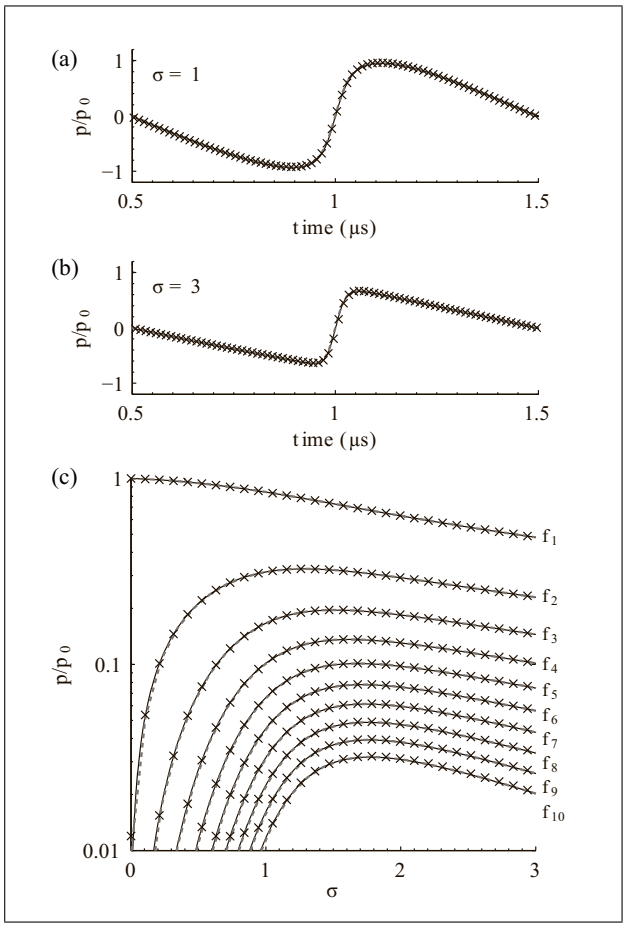

Figure 9. (a) Waveforms at $\sigma = 1$ and (b) $\sigma = 3$ for thermo-viscous attenuation ($\gamma = 2$). Mendousse analytical solution (black line), k-space (gray line) and FDTD numerical solution (markers). (c) Spatial distribution of the first ten harmonics.

the normalized distance $\sigma = x/x_s$; with the parameter of nonlinearity $\beta = 1 + B/2A$ and the acoustic Mach number $\epsilon = v/c_0$, with v is the source particle velocity and k the wavenumber.

Figure 9a,b presents the simulated waveforms at $\sigma = 1$ and $\sigma = 3$ for a Gol'dberg number $\Gamma = 17.4$. The numerical parameters used, same as previous Subsection, lead to grid of $N_\lambda = 115$ elements per wavelength at 1 MHz and a CFL number of 0.62. The wave steepening due to nonlinear processes in the absence of dispersion is well resolved by the numerical method. Figure 9c shows the amplitude of the first ten harmonics for the numerical and the analytic solution as a function of the normalized distance, σ. In addition, the solution was compared also to the obtained by a k-space method applied to the constitutive relations, i.e. the k-wave algorithm [36]. This method was selected due to the low numerical dispersion and the possibility of including frequency power law attenuation. The results of both computational methods and the analytical Mendousse solution [43] agree over al he spectral components analyzed, showing convergence to the analytic solution. In practical ultrasound simulations a grid of $N_\lambda = 115$ elements per wavelength leads to a huge amount of memory resources and computational times. We observe that the relative error of the computational method decreases due to grid coarsening following a square law. The numerical scheme provides therefore second order accuracy, similar to the standard FDTD method. The magnitude of the error mainly depends on the number of elements per wavelength but, due to not ideal dispersion, also on the traveled propagated distance. Including the correction of dispersion by artificial relaxation, for a path length of 100 λ, a grid of 26 elements per wavelength at fundamental frequency was needed to obtain a relative error below 1% for the third harmonic. Obviously, the relative error of the first and second harmonics will be always lower, i.e. the fundamental component error was 0.072%. Provided the second order accuracy of the method, the choice of the number of elements per wavelength depends on the desired precision. For weakly nonlinear problems, grid refinement increases precision an accurate solution is found for 26 elements per wavelength.

However, if the nonlinear problem involves a Gol'dberg ratio much greater than unity, the number of harmonics included in the calculation should be increased significantly. It is worth noting here that the present method improves stability when shock waves are present, but this does not imply that shock waves are accurately described. In this way, the selection of the number of points per wavelength depends also on the magnitude of the nonlinear effects.

This convergence tests were done for thermo-viscous fluids. The most interesting case concerning the scope of the paper is the frequency power law attenuation, but as no analytical solution is available, in the next subsection we compare directly the numerical solution with the k-space solution.

5.3.2. Dispersive media

In the case of frequency power law attenuation media with $\gamma \in [1, 2)$ no general analytic solution exist in nonlinear regime for monochromatic progressive waves. Thus, in order to study convergence in this regime, the proposed FDTD solution was compared with the solution obtained by k-space methods [36]. By using same physical and grid parameters in both methods, the solutions agrees for different power laws. Thus, Figure 10a-b shows a good agreement for the waveform simulated at $\sigma = 1$ and $\sigma = 3$ obtained for $\gamma = 1.6$ and $\Gamma = 17.4$, where the numerical parameters used leads to grid of $N_\lambda = 115$ elements per wavelength at 1 MHz. Here, the characteristic asymmetry on the waveform due to *anomalous* dispersion is observed, in a similar way as in other dispersive media (e.g. mono-relaxing media or sound dispersion induced by boundary layer effects in ducts [25]). In these cases, the shock front after the rarefaction phase is followed by a rounded positive compression profile. The spatial distribution for each harmonic for $\gamma = 1.6$ is shown in Figure 10c, where it is observed that the proposed FDTD solution with optimized attenuation and dispersion converges to the obtained by pseudo-spectral methods up to ten harmonics. As in the case of frequency squared media, grid refinement numer-

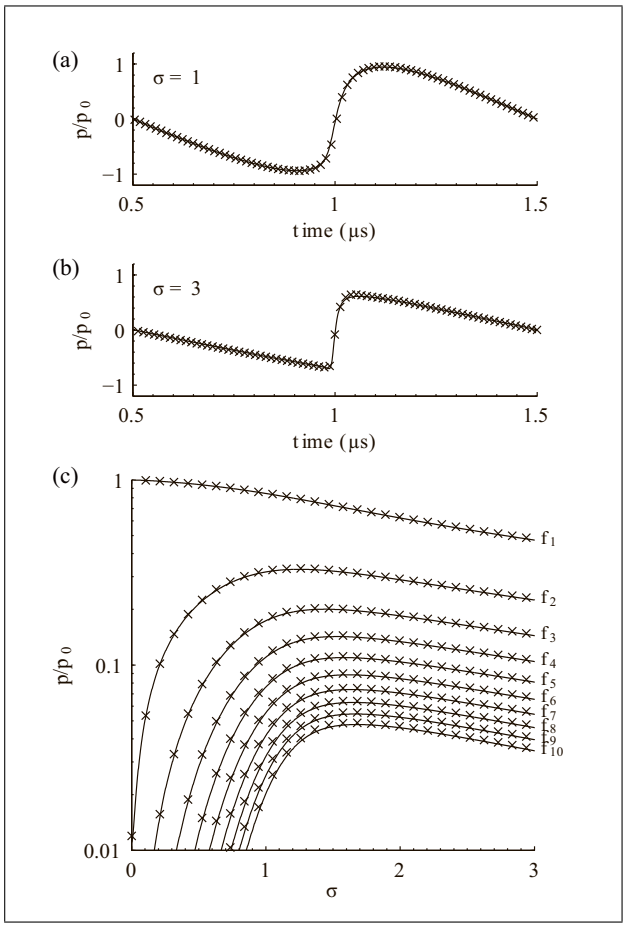

Figure 10. (a) Waveforms at $\sigma = 1$ and (b) $\sigma = 3$ in a tissue-like media with frequency power law ($\gamma = 1.6$). k-space (gray line) and FDTD numerical solution (markers). (c) Spatial distribution of the first ten harmonics.

ical tests have reported a second order accuracy of the FDTD method in the nonlinear regime.

5.4. Nonlinear propagation in tissue-like media including diffraction

5.4.1. Experimental validation

An experiment was designed to test the validity of the algorithm for intense beams in frequency power law attenuation media. The source was formed by a plane single element piezoceramic crystal (PZ 26, Ferroperm Piezoceramics, Denmark) mounted in a custom designed steel housing and a polymethyl methacrylate (PMMA) focusing lens with aperture $A = 50$ mm and radius of curvature $R = 50$ mm. The source was driven with a sinusoidal pulse burst of frequency $f_0 = 1.112$ MHz and $n = 50$ cycles using a function generator (14 bits, 100 MS/s, model PXI5412, National Instruments) and a linear RF amplifier (ENI 1040L, 400W, 55dB, ENI, Rochester, NY). The pressure waveforms were acquired with a HNR 500 μm needle PVDF hydrophone (Onda Corp, CA), and a digitizer (64 MS/s, model PXI5620, National Instruments) was used. A three-axis micropositioning system (OWIS GmbH, Germany) was used to move the hydrophone in three orthogonal directions with an accuracy of 10 μm. The amplitude frequency response of the hydrophone was compensated in post-processing but not in phase due to the absence of phase calibration for this equipment. A scheme of the measurement setup is shown in Figure 11.

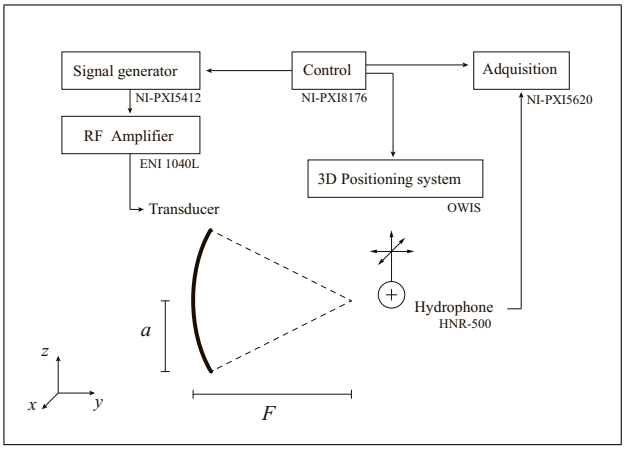

Figure 11. Scheme of the experimental setup.

The source was completely immersed in a castor oil tank (350×350×350 mm). We select this frequency power law attenuation media due to the low variability of its acoustic properties along the existent literature [34, 54]. Using a sound speed inside the bulk of the lens $c_l = 2711$ m/s, and a sound speed of the castor oil of $c_0 = 1480$ m/s (at 26° C room temperature), the effective lens geometrical focal is estimated as $F = R/(1 - c_0/c_l) = 110.1$ mm, leading to a linear lossless gain of $G = 13.4$.

On the other hand, a nonlinear simulation including diffraction and frequency power law attenuation with same parameters was carried out in a workstation (20 cores Intel Xeon E5-2680 CPU, 2.8GHz with 256 GB RAM). The castor oil parameters at 26° C room temperature [54], were $c_0 = 1480$ m/s, $\rho_0 = 961$ kg/m^3, $\alpha = 0.4$ dB/cm/MHz$^\gamma$, $\gamma = 1.69$, $B/A = 12.0$. The grid parameters were $\Delta r = \Delta z = 29.6$ μm and $\Delta t = 13.6$ ns, leading to CFL= 0.96 and $N_\lambda = 45$ elements per wavelength at fundamental frequency, note that this grid leads to $N_\lambda = 15$ for the third harmonic. The boundary conditions were implemented for a spherical focused ultrasound source in the Cartesian lattice. The fine discretization used captures the curvilinear geometry and avoids the spurious reflections due to the rectangular-staircase shaped geometry.

The balance between nonlinear effects and power law attenuation can be estimated by using the Gol'dberg ratio, $\Gamma = x_a/x_s$ where x_s is the shock formation distance and x_a the media attenuation characteristic length. Thus, the amplitude of the source was selected to obtain a Gol'dberg ratio of $\Gamma = 0.25$ in order to let the frequency power law attenuation effects dominate over nonlinear effects. On the other hand, the ratio between diffraction effects and nonlinear effects can be described by the so called Khokhlov number [41] as $N_K = x_s/x_d$, where $x_d = ka^2/2$ is the diffraction length and a the source radius. For the proposed test a Khokhlov number of $N = 0.5$ was selected

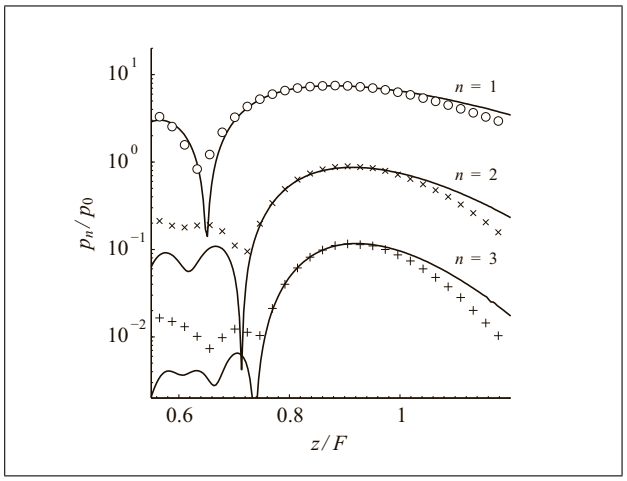

Figure 12. Spatial distribution of the fundamental (∘), second (×) and third (+) harmonic obtained by the numerical (continuous line) and experimental methods (markers) for a focused ultrasound transducer immersed in castor oil.

to let the nonlinear effect slightly dominate over diffraction effects. The selected excitation pressure amplitude was $p_0 = 87.7$ kPa. In order to know the excitation pressure at the transducer surface, the acoustic field in pure water was measured in the small amplitude regime along the acoustic axis. Then, the pressure at the source surface was recovered by fitting the analytical solution of a focused radiator [55] to the axial experimental data as done in [56].

The results are summarized in Figure 12, where axial pressure distribution for the fundamental, second and third harmonic are presented. A good agreement is found between simulations and the experimental test in the focal area. Far to the focal point there exist differences between computations and experiments. These discrepancies can be caused by nonuniform vibration of the piezoelectric source [57], boundary effects of the PMMA lens or missalignment between the source acoustic axis and micropositioning system along the 100 mm axial measurement.

The maximum amplitudes of the first harmonic were $p_{e1} = 0.6539$ MPa for the experiment and $p_{n1} = 0.6576$ for the numeric. The second harmonic peak pressure was $p_{e2} = 78.368$ kPa and $p_{n2} = 76.272$ kPa, and the third harmonic peak pressure $p_{e3} = 10.146$ and $p_{n3} = 10.252$ kPa for the experimental and numeric respectively. The relative errors between numerical and experimental results, calculated at the focal spot, are 0.56% for the fundamental frequency, 2.67% for the second harmonic and 1.04% for the third. No error estimation was done for the peak pressure due to the absence of a phase calibration of the hydrophone.

5.4.2. Highly focused beam

In order to test the algorithm in the nonlinear regime with realistic human tissue parameters a focused bowl of geometrical focal $F = 50$ mm and aperture $A = 50$ mm, driven by a sinusoidal pulse burst of central frequency $f_0 = 1$ MHz and 8 cycles was simulated. These parameters

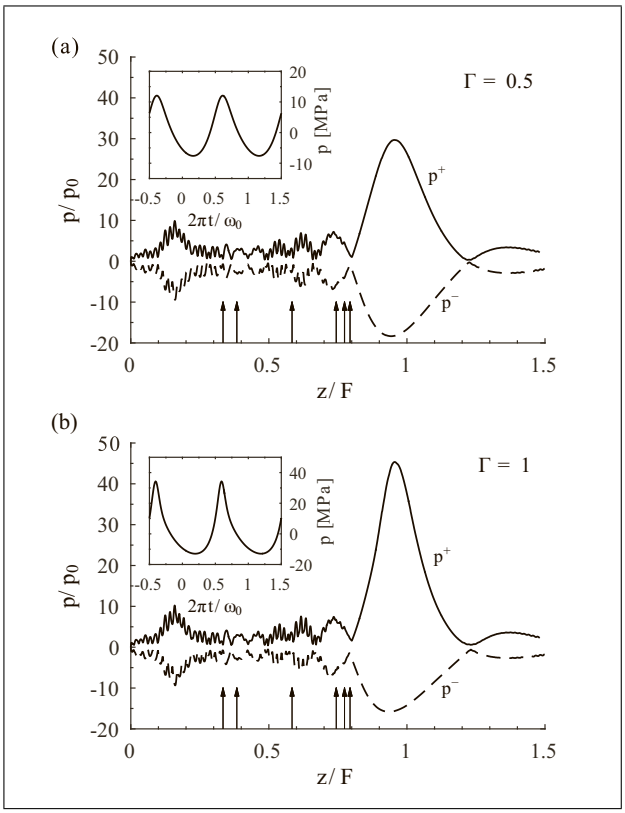

Figure 13. Axial spatial distribution of the peak compression (p^+) and minimum rarefaction (p^-) pressure for a focused beam propagating through a multilayer media. (a) Weakly nonlinear propagation ($\Gamma = 0.5$) and (b) strong nonlinear propagation ($\Gamma = 1$). The insets show the waveforms simulated at the geometrical focal. The arrows indicate the boundaries of the tissue layers.

lead to a source gain $G = 26.5$ and a $f_{\text{number}} = 1$, therefore, the source is beyond the paraxial limit and KZK models are not accurate to describe the acoustic field. The simulation was performed in a multilayer configuration with realistic tissue parameters. The simulated medium is formed by seven layers. The first layer, where the source was located, was water at 20° C. The multilayer media, a simplified model of an abdominal wall, was placed at 10 mm from the source boundary. The first layer was 2.5 mm of human skin tissue, the second one 10 mm of fat, then 8 mm of abdominal muscle, 1.5 mm of fat, 1 mm of connective tissue and finally 40 mm of human liver. Therefore, the focal spot was located inside the liver tissue layer. The parameters of the different tissues are listed in Table III. The numerical grid parameters were $\Delta r = \Delta z = 29.6$ μm and $\Delta t = 11.9$ ns, leading to CFL= 0.84 and $N_\lambda = 50$ elements per wavelength at fundamental frequency ($N_\lambda = 17$ for third harmonic).

Figure 13 shows the spatial peak pressure profiles for different excitation amplitudes. The arrows indicate the boundary of the layers. The lowest initial amplitude simulated, shown in Figure 13a, was $p_0 = 0.45$ MPa, while in Figure 13b the amplitude was increased to $p_0 = 0.91$ MPa. Figure 13a presents results for $\Gamma = 0.5$ and $N_{\text{K}} = 0.26$, which indicates that the attenuation effects dominates over

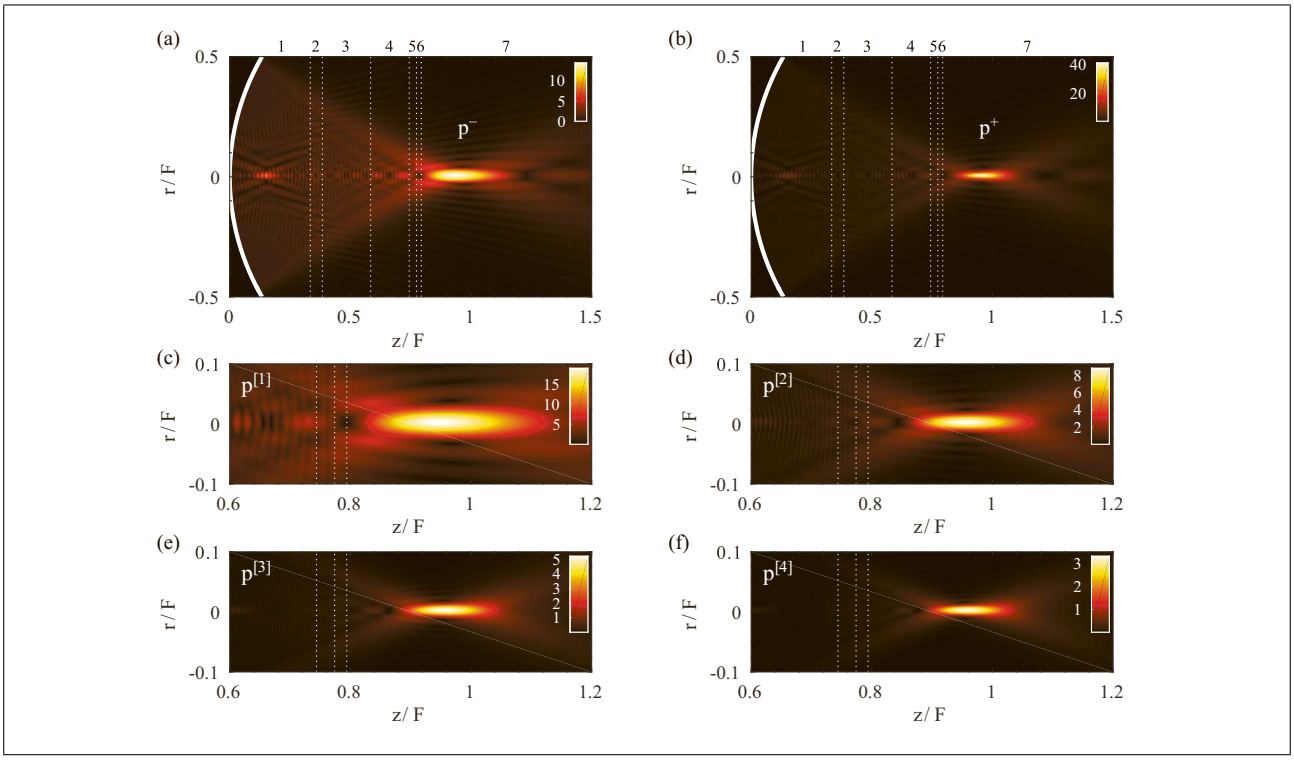

Figure 14. (Colour online) (a) Spatial distribution of the minimum rarefaction (p^-) pressure and (b) peak compression (p^+) and for a focused beam propagating through a multilayer tissue media for $\Gamma = 1$. The boundaries between layers are marked with white dashed lines and the source is sketched in solid white line. Colour scale units are MPa. Corresponding field of the (c) first, (d) second, (e) third, (f) fourth harmonic at the focal area.

nonlinear effects and nonlinearity dominates over diffraction effects. In this way, low asymmetry is observed between the positive compression peak, p^+, and the minimum rarefaction pressure distribution, p^-. The calculated waveform at $z = F$, shown in the inset of Figure 13a, is weakly distorted. However, there exist differences between its normalized peak amplitude $p^+/p_0 = 29.6$ and $p^-/p_0 = 18.3$, and the source characteristic linear gain, $G = 26.4$. They are caused, on the one hand by the attenuation effects, where the value of the lossy linear gain observed was $G_\alpha = p^+/p_0 = p^-/p_0 = 21.2$ measured at $z = F$, i.e. the amplitude at the focal was reduced to 80.2% of the lossless amplitude. On the other hand, the differences due to the asymmetry between compression and rarefaction cycles are caused by the combined effect of nonlinearity and focusing.

If source amplitude is increased to $p_0 = 0.91$ MPa, as shown in Figure 13b, the ratio between attenuation and nonlinear effects is increased to $\Gamma = 1$. In this regime, nonlinear effects are of the same order as attenuation effects. On the other hand, increasing source amplitude while keeping same transducer parameters implies also the Khokhlov number changes to $N_K = 0.13$, so the nonlinearity clearly dominates over diffraction effects. In this regime, highly asymmetric pressure distribution is observed, where the values at focal point are $p^+ = 45.34$ MPa and $p^- = -15.81$ MPa.

Other typical nonlinear phenomena characteristic of high intensity focused sources can also be observed: formation of sharp shock fronts and its corresponding harmonic generation, or, as Figures 14a-b shows for $\Gamma = 1$, narrowing of the beam for p^+ and broadening for p^- pressure distributions. In addition, nonlinear focal shift, i.e. displacement of the peak pressure relative to the position of the linear peak pressure can be also predicted for tissue propagation. In the case of $\Gamma = 1$ it was observed a nonlinear focal shift $\Delta F^+ = +0.60$ mm and $\Delta F^- = -0.93$ mm for the p^+ and p^- pressure distribution, respectively. The corresponding pressure spatial distribution for the first four harmonics is shown in Figures 14c-f for $\Gamma = 1$. It can be observed the narrowing of the higher spectral components over the focal spot in both, axial and lateral dimension. It can be seen also the formation of secondary focal spots around $z/F = 0.2$ due to the back-reflection of waves by the tissue layers.

Table III. Parameters of the multilayer tissue. c_0 in [m/s], ρ_0 in [kg/m^3], α in [dB/cm].

Tissue	c_0	ρ_0	B/A	α	γ
Water	1482	1000	4.9	$2.17{\cdot}10^{-3}$	2.0
Skin [51, 58, 59]	1640	1090	7.9	0.70	0.6
Muscle [51, 60, 59]	1547	1050	7.0	1.09	1.0
Fat [51, 60, 59]	1480	950	10.0	0.48	1.1
Connective [60, 59]	1613	1120	7.0	1.57	1.2
Liver [51, 61, 59]	1600	1060	6.7	0.50	1.4

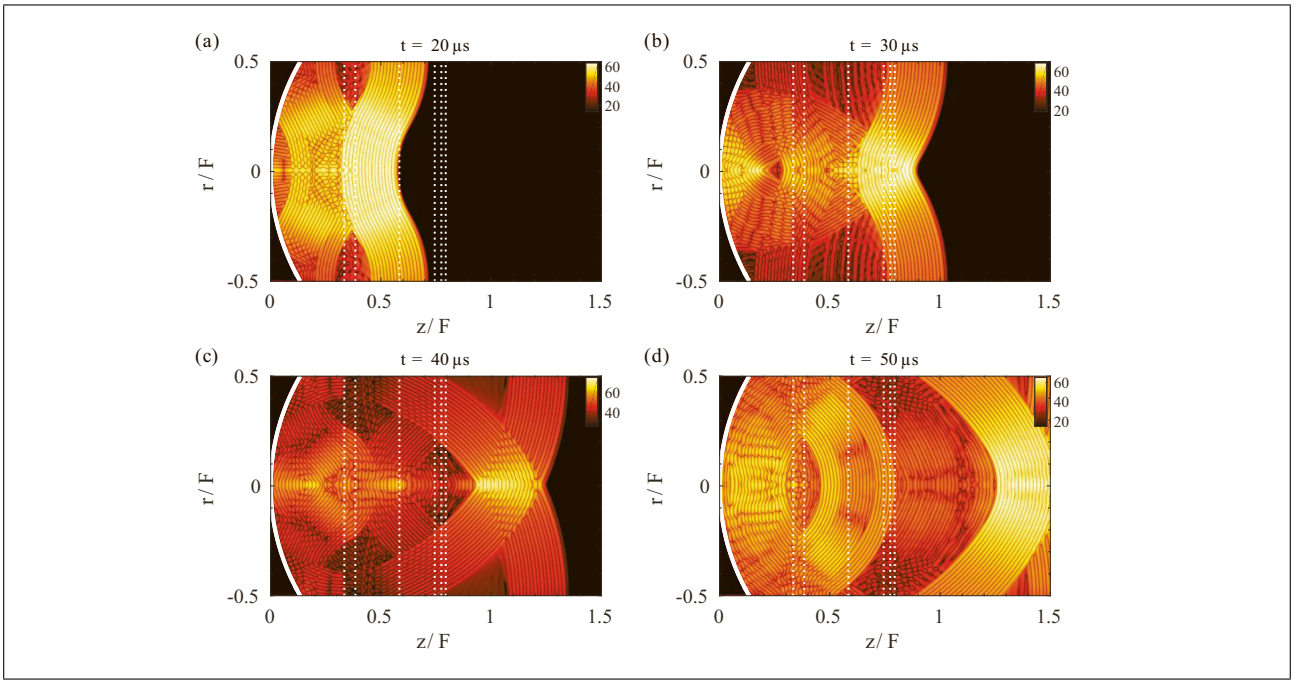

Figure 15. (Colour online) Pressure distribution at instants (a) $t = 20\,\mu$s, (b) $t = 30\,\mu$s (c) $t = 40\,\mu$s and (c) $t = 50\,\mu$s for the focused beam propagating through a multilayer tissue media for $\Gamma = 1$. The boundaries between layers are marked with white dashed lines and the source is sketched in solid white line. Colourbar in logarithmic scale $10\log_{10}|p|$ with p in Pa units.

Finally, Figure 15 shows the pressure distribution at different instants. In Figure 15a, $t = 20\,\mu$s, it can be observed the back-reflection of the pulse at the interface between water and the first tissue layers, skin and fat. As the impedance contrast between layers is relatively low, most of the energy is transmitted. Then, in Figure 15b, $t = 30\,\mu$s, the transmitted wavefront start to focus around the geometrical focal. However, it can be noticed that the field becomes complex due to the multiple reflections between layers. In addition, it can be seen how the first back-reflected component returns to the source and, then, is reflected again by the curvilinear shape of the transducer. In Figure 15c, $t = 40\,\mu$s, it is observed how this component focus again around $z/F = 0.2$, in addition to the main focal spot around the geometrical focus. Finally, in Figure 15d, $t = 50\,\mu$s it can be observed how some energy remains inside the multilayer system after the main pulse diverges. The interactions of backward and forward waves cause ripples in the total field as shown previously in Figure 14. It is worth noting here that these multiple reflections in a multilayer media leads to dispersion. As the wavelength is smaller than the layer thickness, this dispersion will be not negligible. The induced dispersion by the multiple reflections, which are captured by the full-wave method, can modify the harmonic generation processes, as it has been reported recently for multilayer acoustic media [62].

6. Summary and conclusions

A general model based on the full constitutive relations of nonlinear acoustics in relaxing media have been presented in a time-domain formulation which does not require convolutional operators. A numerical solution by means of finite-differences in time-domain have been obtained, showing that the theoretical attenuation and dispersion due to relaxation processes can be achieved by the numerical method with accuracy. These results can be also used to model typical relaxation process of other relaxing media (e. g. the processes observed in air, associated to the molecules of oxygen and nitrogen, or in seawater, associated to the relaxation of boric acid and magnesium sulfate).

Moreover, a method for modeling frequency power law attenuation by means of multiple relaxation has been implemented in the constitutive relations. The proposed method can describe local variations of the exponent of the frequency power law, so that an arbitrary attenuation curve in the range $0 < \gamma < 2$ can be modeled by means of the proper optimization of the relaxation coefficients. This feature of the presented method is advantageous compared with most fractional derivatives methods, where the attenuation follows an exact but unique frequency power law over the entire frequency range. A broad range of human tissues have been modeled and the accuracy of the fit using from two to four relaxation processes has been discussed.

Furthermore, a computational technique that exploits the *anomalous* dispersion of the relaxation processes is employed to mitigate the numerical dispersion of the finite-differences scheme. Thus, while phase speed is corrected by including artificial relaxation processes, its corresponding artificial attenuation is used to improve stability in the nonlinear regime. In this way, smooth and stable versions of shock waves have been obtained and compared

favorably with an analytic solution. Furthermore the validity of the algorithm including diffraction has been tested with experimental measurements of a focused beam in castor oil.

As the model is developed from the constitutive relations for nonlinear acoustics, most wave phenomena is captured. As for the difference with one-way models, the proposed model implicitly includes multiple wave direction, and, due to the Lagrangian density of acoustic energy is implicitly included in the computation, multiple scattering and strong resonance effects can be, in theory, accurately described. Moreover, unlike KZK and other parabolic approximations, the proposed model captures the diffraction exactly. The field of acoustic beams simulated by the present method is not approximated only to the beam axis, but also in the near field and far to the beam axis. Therefore, highly focused devices can be simulated.

The code has shown to be particularly appropriate if the problem to simulate presents axisymmetry, because the constitutive relations for nonlinear acoustics are solved in a computational 2D domain, while standard k-space methods need to employ full 3D domains due to the poor convergence of the Fourier series at discontinuities ($r = 0$). A realistic example would be the focused ultrasound transducer simulated in Section 5.4.2, where a full 3D solution will require huge computational resources and calculation times. Finally, as the particle velocity vector and the acoustic density fields are solved implicitly by the code, this information can be used to estimate other relevant magnitudes such as the full nonlinear intensity vector, the nonlinear acoustic radiation forces in these absorbing media or the acoustic streaming generated in frequency power law attenuation fluids.

Acknowledgement

The authors acknowledge financial support from the FPI program of the Universitat Politècnica de València.

References

[1] M. Verweij, B. Treeby, K. van Dongen, L. Demi: Capter 2.19 - Simulation of Ultrasound Fields. – In: Comprehensive Biomedical Physics. A. Brahme (ed.). Elsevier Science Ltd, Oxford, 2014, 465 – 500.

[2] J. Gu, Y. Jing: Modeling of wave propagation for medical ultrasound: a review. IEEE Trans. Ultrason., Ferroelect., Freq. Control **62** (2015) 1979–1992.

[3] D. Baresch, J.-L. Thomas, R. Marchiano: Three-dimensional acoustic radiation force on an arbitrarily located elastic sphere. J. Acoust. Soc. Am. **133** (2013) 25–36.

[4] S. I. Aanonsen, T. Barkve, J. N. Tjøtta, S. Tjøtta: Distortion and harmonic generation in the nearfield of a finite amplitude sound beam. J. Acoust. Soc. Am. **75** (1984) 749–768.

[5] Y.-S. Lee, M. F. Hamilton: Time-domain modeling of pulsed finite-amplitude sound beams. J. Acoust. Soc. Am. **97** (1995) 906–917.

[6] R. O. Cleveland, M. F. Hamilton, D. T. Blackstock: Time-domain modeling of finite-amplitude sound in relaxing fluids. J. Acoust. Soc. Am. **99** (1996) 3312–3318.

[7] X. Yang, R. O. Cleveland: Time domain simulation of nonlinear acoustic beams generated by rectangular pistons with application to harmonic imaging. J. Acoust. Soc. Am. **117** (2005) 113–123.

[8] V. Khokhlova, A. Ponomarev, M. Averkiou, L. Crum: Nonlinear pulsed ultrasound beams radiated by rectangular focused diagnostic transducers. Acoust. Phys. **52** (2006) 481–489.

[9] Y. Jing, R. O. Cleveland: Modeling the propagation of nonlinear three-dimensional acoustic beams in inhomogeneous media. J. Acoust. Soc. Am. **122** (2007) 1352–1364.

[10] J. E. Soneson, M. R. Myers: Gaussian representation of high-intensity focused ultrasound beams. J. Acoust. Soc. Am. **122** (2007) 2526–2531.

[11] F. Prieur, S. Holm: Nonlinear acoustic wave equations with fractional loss operators. J. Acoust. Soc. Am. **130** (2011) 1125–1132.

[12] P. T. Christopher, K. J. Parker: New approaches to nonlinear diffractive field propagation. J. Acoust. Soc. Am. **90** (1991) 488–499.

[13] J. Tavakkoli, D. Cathignol, R. Souchon, O. A. Sapozhnikov: Modeling of pulsed finite-amplitude focused sound beams in time domain. J. Acoust. Soc. Am. **104** (1998) 2061–2072.

[14] R. J. Zemp, J. Tavakkoli, R. S. Cobbold: Modeling of nonlinear ultrasound propagation in tissue from array transducers. J. Acoust. Soc. Am. **113** (2003) 139–152.

[15] T. Varslot, G. Taraldsen: Computer simulation of forward wave propagation in soft tissue. IEEE Trans. Ultrason., Ferroelect., Freq. Control **52** (2005) 1473–1482.

[16] P. Yuldashev, V. Khokhlova: Simulation of three-dimensional nonlinear fields of ultrasound therapeutic arrays. Acoust. Phys. **57** (2011) 334–343.

[17] I. M. Hallaj, R. O. Cleveland: FDTD simulation of finite-amplitude pressure and temperature fields for biomedical ultrasound. J. Acoust. Soc. Am. **105** (1999) L7–L12.

[18] I. M. Hallaj, R. O. Cleveland, K. Hynynen: Simulations of the thermo-acoustic lens effect during focused ultrasound surgery. J. Acoust. Soc. Am. **109** (2001) 2245–2253.

[19] G. F. Pinton, J. Dahl, S. Rosenzweig, G. E. Trahey: A heterogeneous nonlinear attenuating full-wave model of ultrasound. IEEE Trans. Ultrason., Ferroelect., Freq. Control **56** (2009) 474–488.

[20] J. Huijssen, M. D. Verweij: An iterative method for computation of nonlinear, wide-angle, pulsed acoustic fields of medical diagnostic transducers. J. Acoust. Soc. Am. **127** (2010) 33–44.

[21] L. Demi, K. Van Dongen, M. Verweij: A contrast source method for nonlinear acoustic wave fields in media with spatially inhomogeneous attenuation. J. Acoust. Soc. Am. **129** (2011) 1221–1230.

[22] M. D. Verweij, L. Demi, K. W. van Dongen: Computation of nonlinear ultrasound fields using a linearized contrast source method. J. Acoust. Soc. Am. **134** (2013) 1442–1453.

[23] Y. Jing, T. Wang, G. T. Clement: A k-space method for moderately nonlinear wave propagation. IEEE Trans. Ultrason., Ferroelect., Freq. Control **59** (2012) 1664–1673.

[24] Y. Jing, D. Shen, G. T. Clement: Verification of the Westervelt equation for focused transducers. IEEE Trans. Ultrason., Ferroelect., Freq. Control **58** (2011) 1097–1101.

[25] M. Hamilton, D. Blackstock: Nonlinear acoustics. Academic Press, San Diego, CA 92101, USA, 1998, 455.

[26] C. W. Manry, S. L. Broschat: FDTD simulations for ultrasound propagation in a 2-D breast model. Ultrason. Imaging **18** (1996) 25–34.

[27] T. D. Mast, L. M. Hinkelman, M. J. Orr, V. W. Sparrow, R. C. Waag: Simulation of ultrasonic pulse propagation through the abdominal wall. J. Acoust. Soc. Am. **102** (1997) 1177–1190.

[28] X. Yuan, D. Borup, J. Wiskin, M. Berggren, S. A. Johnson: Simulation of acoustic wave propagation in dispersive media with relaxation losses by using FDTD method with PML absorbing boundary condition. IEEE Trans. Ultrason., Ferroelect., Freq. Control **46** (1999) 14–23.

[29] T. D. Mast, L. P. Souriau, D.-L. Liu, M. Tabei, A. I. Nachman, R. C. Waag: A k-space method for large-scale models of wave propagation in tissue. IEEE Trans. Ultrason., Ferroelect., Freq. Control **48** (2001) 341–354.

[30] B. E. Treeby, B. Cox: Modeling power law absorption and dispersion for acoustic propagation using the fractional Laplacian. J. Acoust. Soc. Am. **127** (2010) 2741–2748.

[31] C. K. Tam, J. C. Webb: Dispersion-relation-preserving finite difference schemes for computational acoustics. J. Comput. Phys. **107** (1993) 262–281.

[32] S. Ginter, M. Liebler, E. Steiger, T. Dreyer, R. E. Riedlinger: Full-wave modeling of therapeutic ultrasound: nonlinear ultrasound propagation in ideal fluids. J. Acoust. Soc. Am. **111** (2002) 2049–2059.

[33] V. W. Sparrow, R. Raspet: A numerical method for general finite amplitude wave propagation in two dimensions and its application to spark pulses. J. Acoust. Soc. Am. **90** (1991) 2683–2691.

[34] M. Liebler, S. Ginter, T. Dreyer, R. E. Riedlinger: Full wave modeling of therapeutic ultrasound: efficient time-domain implementation of the frequency power-law attenuation. J. Acoust. Soc. Am. **116** (2004) 2742–2750.

[35] E. G. Lobanova, S. V. Lobanov, V. A. Khokhlova: Counterpropagation of waves with shock fronts in a nonlinear tissue-like medium. Acoust. Phys. **60** (2014) 387–397.

[36] B. E. Treeby, J. Jaros, A. P. Rendell, B. Cox: Modeling nonlinear ultrasound propagation in heterogeneous media with power law absorption using a k-space pseudospectral method. J. Acoust. Soc. Am. **131** (2012) 4324–4336.

[37] N. Albin, O. P. Bruno, T. Y. Cheung, R. O. Cleveland: Fourier continuation methods for high-fidelity simulation of nonlinear acoustic beams. J. Acoust. Soc. Am. **132** (2012) 2371–2387.

[38] K. Shahbazi, N. Albin, O. P. Bruno, J. S. Hesthaven: Multidomain Fourier-continuation/WENO hybrid solver for conservation laws. J. Comput. Phys. **230** (2011) 8779 – 8796.

[39] B. Lombard, J.-F. Mercier: Numerical modeling of nonlinear acoustic waves in a tube with an array of helmholtz resonators. J. Comput. Phys. **259** (2013) 421–443.

[40] C. Bogey, C. Bailly: A family of low dispersive and low dissipative explicit schemes for flow and noise computations. J. Comput. Phys. **194** (2004) 194–214.

[41] K. Naugolnykh, L. Ostrovsky: Nonlinear wave processes in acoustics. Cambridge University Press, 40 West 20th Street, New York, NY 10011-4211, USA, 1998, (Cambridge Texts in Applied Mathematics), 298.

[42] O. Rudenko, S. Soluyan: Theoretical foundations of nonlinear acoustics. Consultants Bureau, New York, NY 10011, USA, 1977, (Studies in Soviet science), 274.

[43] A. Pierce: Acoustics: An introduction to its physical principles and applications. Acoustical Society of America, Melville, New York, NY 11747-4502, USA, 1989, 678.

[44] K. S. Yee et al.: Numerical solution of initial boundary value problems involving Maxwell's equations in isotropic media. IEEE Trans. Antennas Propag **14** (1966) 302–307.

[45] D. Botteldooren: Numerical model for moderately nonlinear sound propagation in three-dimensional structures. J. Acoust. Soc. Am. **100** (1996) 1357–1367.

[46] R. LeVeque: Numerical methods for conservation laws. Birkhauser Verlag, 133 CH-4010 Basel, Switzerland, 1992, 214.

[47] Q.-H. Liu, J. Tao: The perfectly matched layer for acoustic waves in absorptive media. J. Acoust. Soc. Am. **102** (1997) 2072–2082.

[48] Q. H. Liu: Perfectly matched layers for elastic waves in cylindrical and spherical coordinates. J. Acoust. Soc. Am. **105** (1999) 2075–2084.

[49] A. Polyakova, S. Soluyan, R. Khokhlov: Propagation of finite disturbances in a relaxing medium. Sov. Phys. Acoust **8** (1962) 78–82.

[50] K. R. Waters, J. Mobley, J. G. Miller: Causality-imposed (Kramers-Kronig) relationships between attenuation and dispersion. IEEE Trans. Ultrason., Ferroelect., Freq. Control **52** (2005) 822–823.

[51] C. Hill, J. C. Bamber, G. ter Haar: Physical principles of medical ultrasonics, 2nd ed. John Wiley & Sons Ltd, Chichester, West Sussex PO19 8SQ, England, 2004, 528.

[52] M. O'Donnell, E. T. Jaynes, J. G. Miller: Kramers–Kronig relationship between ultrasonic attenuation and phase velocity. J. Acoust. Soc. Am. **69** (1981) 696–701.

[53] N. Jiménez: Nonlinear acoustic waves in complex media. Dissertation. Universitat Politècnica de València, 2015.

[54] B. E. Treeby, B. T. Cox, E. Z. Zhang, S. K. Patch, P. C. Beard: Measurement of broadband temperature-dependent ultrasonic attenuation and dispersion using photoacoustics. IEEE Trans. Ultrason., Ferroelect., Freq. Control **56** (2009) 1666–1676.

[55] H. T. O'Neil: Theory of focusing radiators. The Journal of the Acoustical Society of America **21** (1949) 516–526.

[56] F. Camarena, S. Adrián-Martínez, N. Jiménez, V. Sánchez-Morcillo: Nonlinear focal shift beyond the geometrical focus in moderately focused acoustic beams. J. Acoust. Soc. Am. **134** (2013) 1463–1472.

[57] M. S. Canney, M. R. Bailey, L. A. Crum, V. A. Khokhlova, O. A. Sapozhnikov: Acoustic characterization of high intensity focused ultrasound fields: A combined measurement and modeling approach. J. Acoust. Soc. Am. **124** (2008) 2406–2420.

[58] C. Moran, N. Bush, J. Bamber: Ultrasonic propagation properties of excised human skin. Ultrasound in medicine & biology **21** (1995) 1177–1190.

[59] T. D. Mast: Empirical relationships between acoustic parameters in human soft tissues. Acoustics Research Letters Online **1** (2000) 37–42.

[60] T. D. Mast, L. M. Hinkelman, L. A. Metlay, M. J. Orr, R. C. Waag: Simulation of ultrasonic pulse propagation, distortion, and attenuation in the human chest wall. The Journal of the Acoustical Society of America **106** (1999) 3665–3677.

[61] C. Sehgal, G. Brown, R. Bahn, J. F. Greenleaf: Measurement and use of acoustic nonlinearity and sound speed to estimate composition of excised livers. Ultrasound in medicine & biology **12** (1986) 865–874.

[62] N. Jiménez, A. Mehrem, R. Picó, L. M. García-Raffi, V. Sánchez-Morcillo: Nonlinear propagation and control of acoustic waves in phononic superlattices. Comptes Rendus Physique **17** (2 2016) 543 – 554.